Radiation Physics and Chemistry 130 (2017) 442–450

Contents lists available at ScienceDirect

Radiation Physics and Chemistry

journal homepage: www.elsevier.com/locate/radphyschem

Silver nanoparticles in X-ray biomedical applications

Facundo Mattea[a,b,*], José Vedelago[b,c], Francisco Malano[b,c], Cesar Gomez[a], Miriam C. Strumia[a], Mauro Valente[b,c,d,e]

[a] Departamento de Química Orgánica, Facultad de Ciencias Químicas, Universidad Nacional de Córdoba, CONICET, Córdoba, Argentina
[b] Laboratorio de Investigación e Instrumentación en Física Aplicada a la Medicina e Imágenes de Rayos X (LIIFAMIRx), Universidad Nacional de Córdoba, Córdoba, Argentina
[c] Instituto de Física Enrique Gaviola (IFEG) – CONICET, Córdoba, Argentina
[d] Departamento de Ciencias Físicas, Universidad de La Frontera, Temuco, Chile
[e] Centro de Física e Ingeniería en Medicina (CFIM), Universidad de la Frontera, Temuco, Chile

ARTICLE INFO

Keywords:
Silver
Nanoparticles
Fluorescence
X-ray
Monte Carlo
Simulation

ABSTRACT

The fluorescence of silver nanoparticles or ions can be used for detection and dose enhancement purposes in X-ray irradiation applications. This study is focused on the full integration of the chemical synthesis of silver nanoparticles suitable for dosimetric and radiological purposes with characteristics that can be exploited in radiotherapy and radiodiagnostic. A narrow size distribution and a compatible stabilizing agent is often desired in order to obtain homogeneous behaviors in nanoparticle suspension. With the method proposed in this study, nanoparticles ranging from 5 to 20 nm were obtained. The fluorescence of aqueous suspensions of silver nanoparticles has been measured experimentally and simulated with the Monte Carlo PENELOPE code for different silver concentrations and geometrical configurations. Finally, the feasibility of using these nanoparticles for the elaboration of Fricke gel dosimeters has been tested obtaining a dose enhancement when compared with the same material irradiated below the silver K-edge.

1. Introduction

Particles in the size range 1–100 nm are commonly referred as nanoparticles (NPs) and have been gaining a great interest and application in many research areas, such as food industry (Pan and Zhong, 2016), material science (Linic et al., 2015; Wildgoose et al., 2006) and most of the current health applications (Barreto et al., 2011; Thakor et al., 2011; Weissleder et al., 2014; Yamada et al., 2015). These materials have unique characteristics (Mohanraj et al., 2006; Nie et al., 2010) and one of the great advantages of using NPs is the ability to vary these characteristics by modifying their size, size distribution, shape, and surface chemistry. Moreover, many physicochemical properties such as photochemical characteristics, magnetic properties or fluorescence can be changed by these variations and also by selecting a specific preparation method. Also, in most cases, it is possible to obtain materials which behave differently from their bulk version (Sau et al., 2010).

The first application of NPs in medicine and medical research took place in the early 1950s, which were based on liposomes and polymer systems for drug delivery, protecting the drugs and providing them with hydrophilic or hydrophobic functionality when needed (Petros and DeSimone, 2010). From that moment to the present great advances have been made in the use of NPs into medicine and at least 20 therapeutics with NPs have clinical use. In addition, numerous NPs platforms are currently under preclinical and clinical development including liposomes, polymeric micelles, dendrimers, quantum dots, gold and ceramic NPs (Schütz et al., 2013). One of the medical areas where NPs had a great impact is in treating complex diseases such as cancer. In most cases, a single approach or treatment is not sufficient and a combination of chemotherapy, radiotherapy, immunotherapy, gene therapy and thermotherapy is used to treat the disease. NPs are ideal platforms for a synergic combination of chemo and radiotherapy since they can act as contrast agents and drug carriers simultaneously (Puntes, 2016; Smith et al., 2012). Also, NPs of high Z number atoms like gold, gadolinium and iodine have been used for decades as radiological sensitizers and contrast agents (Rancoule et al., 2016). A key goal in radiotherapy is to increase the radiation dose deposited in the target tissue while minimizing the dose to surrounding healthy tissues. From a general point of view, absorbed dose is a consequence of primary beam, scattering particles and eventually –as happen in mixed field situations– secondary radiation produced by the primary beam. In this context, dose components associated with these secondary radiations may be considered as dosimetric reinforcement or dose enhancement. Actually, dose enhancement at interfaces between high

* Corresponding author at: Departamento de Química Orgánica, Facultad de Ciencias Químicas, Universidad Nacional de Córdoba, CONICET, Córdoba, Argentina.

http://dx.doi.org/10.1016/j.radphyschem.2016.10.008
Received 16 August 2016; Received in revised form 8 October 2016; Accepted 8 October 2016
Available online 11 October 2016
0969-806X/

and low atomic number materials has been largely studied (Botchway et al., 2015; Hainfeld et al., 2004). The presence of metallic NPs with high atomic number in biological tissues have proved a promising performance as radiosensitizers for both kilo-voltage and mega-voltage regimens (Guidelli and Baffa, 2014; Jones et al., 2010). In one of the first studies in the field Nath et al. (1990) incorporated iodine into cellular DNA with iododeoxyuridine in vitro, reporting an approximate radiation enhancement factor of 3 times, whereas Regulla et al. (1998) reported dose enhancement factors of about 50 times for fibroblast irradiated on a gold foil. Furthermore, it is possible to take advantage from the increased mass absorption coefficient of high atomic number NPs with the aim of enhancing radiation damage mainly due to secondary electrons and free radical species, which would yield appreciable factors for radiosensitization enhancement, even for modest or relatively low concentrations of NPs.

With a different approach, high atomic number materials like gadolinium and iodine have been used as contrast agents (Caschera et al., 2016; Taupin et al., 2015). There are several studies reporting that these agents are capable of in vitro and in vivo damage when are used combined with ionizing radiation (Coppola et al., 1984; McMahon et al., 2011; Sancey et al., 2014). Because of the high atomic number of metallic NPs, it appears obvious that they are candidates as potential contrast agents. These applications may become more relevant if targeting efficacy can be achieved, thereby limiting the cost implications while therapeutic outcome is improved due to a better target specificity. What is more, this capability has given place to new imaging techniques, such as X-ray fluorescence computed tomography (Kuang et al., 2013).

In this study silver NPs were synthesized to investigate the relationship between fluorescence signals with silver concentration and depth in a tissue equivalent phantom. To synthesize these particles two main approaches can be used, top down methods like milling or grinding and bottom-up approaches (Sau and Rogach, 2010) where the nanomaterials are synthesized from a solution by means of chemical reactions or precipitation techniques. The former approach usually renders poorly controlled properties with a behavior similar to the bulk material, while the latter approach could lead to completely new functionalities and physicochemical properties (Lee et al., 2016). Among the different synthesis methods available in literature a thermal reduction of silver nitrate within a gelatin matrix was used. The main idea of using gelatin as a stabilizing agent for the silver NPs suspension was to ensure a maximum compatibility with the matrix of most of the 3D dosimetric systems e.g. polymer or Fricke gel. The Fricke gel dosimeter is an acid solution doped with ferrous ions (Fe^{2+}) within a gelatin or agarose supporting matrix. The absorbed dose in this material can be correlated to the amount of ferrous ion oxidized by water radicals formed by radiolysis during an irradiation (Schreiner, 2004). The use of silver NPs in Fricke gel dosimeters has not been reported yet; however, there are some reports on gel dosimetry with NPs (Titus et al., 2016). Moreover, special precautions have to be taken into account when using silver ions as a dopant, since a redox reaction between silver and ferrous ions can take place.

The main goal of this study is the synthesis and use of silver NPs for dosimetry and radiological applications from a theoretical and experimental standpoint. For that purpose, the fluorescence signal of silver was used for the detection of volumes doped with silver NPs at different depths and Ag concentrations. Also, another specific objective was to develop a useful tool to simulate and predict the fluorescence of silver in tissue equivalent material. Finally, the feasibility of using these NPs in Fricke gel dosimeters for dose enhancement estimation was tested.

2. Materials and methods

2.1. Nanoparticle synthesis

Silver nitrate 99.9% acquired from Prodesa S.C.A. (Buenos Aires, Argentina) was thermally reduced against the amino groups present in porcine gelatin 300 Bloom purchased from Sigma Aldrich (Saint Louis, MO, USA) according to the reaction schemed in Fig. 1 in an aqueous media. In the presence of amino groups such as the ones in amino acids and proteins, silver ions form complexes ensuring their homogeneous distribution in the reaction media. Once temperature conditions provide the necessary energy, the reduction of silver ions takes place under isothermal conditions, where the growth of NPs is delayed by reducing the ion diffusion mainly given by the coordination between silver ions and the amino groups. For that purpose, gelatin and silver nitrate concentration and reaction time depicted in Table 1 were used at a temperature of 90 °C in closed vessels at a pressure of 0.6 atm.

2.2. Nanoparticle characterization

The size and morphology of the silver NPs were characterized by transmission electron microscopy (TEM) of the reaction products. After the reaction time was completed, a sample of each reaction product, a colloidal solution, was diluted 10 times with water, then 2 drops of the obtained solution were placed on a TEM grid and dried at room temperature. Afterwards, TEM micrographs of at least 10 different random regions of the grid were collected and analyzed using the procedure described elsewhere (Rice et al., 2013) with a Jeol - 1200 EXII TEM. Briefly, the procedure consists on using the open source software ImageJ, with a set of analysis routines (http://rsbweb.nih.gov/ij/download.html) following these steps: first setting the scale of the image to match the TEM micrograph scale. Secondly, cropping the image to remove additional information such as scale bars, correct contrast and brightness to ensure that all images have an centered histogram and wide enough to cover 80% of the possible grey levels. Then, performing a threshold operation and select the desired shape descriptors and finally analyzing the particles. In the present study. the Ferret's diameter and the diameter of a circle with equivalent area were used to represent the size distribution and morphology of the obtained NPs. Afterwards, the statistical analysis of the results was performed with the statistical toolbox in Matlab® version 7.11.0.584 (R2010b) 64 bit (MathWorks Inc, Natick, MA, USA).

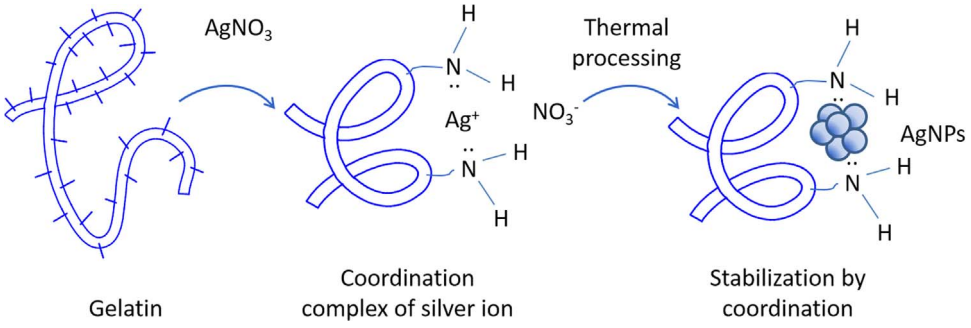

Fig. 1. Synthesis of silver NPs by a thermal reduction reaction of silver ions and gelatin.

Table 1
Silver nanoparticle synthesis conditions.

VARIABLE	RANGE	
TEMPERATURE	90	°C
$AgNO_3$ CONCENTRATION	0.005–0.05	M
GELATIN 300 BLOOM CONCENTRATION	1	% w/w
REACTION TIME	15	h

2.2.1. X-ray irradiation

Two different setups were used in this study, first aqueous samples containing either silver nitrate or a suspension of silver Nps were placed inside polymethylmethacrylate (PMMA) cuvettes within a polyethylene terephthalate (PET) phantom. These samples were irradiated in an X-ray tube with a W anode connected to a generator with a maximum power of 3 kW, the tube output has a 94 μm Zirconium filter and a 4 mm Aluminum filter. In the first setup the fluorescence of silver was detected using an electrical current of 5 mA and a voltage of 50 kVp, a source-to-phantom distance of 930 mm, field size of 30×30 mm^2 and a collimator to sample distance of 135 mm. The scattered spectrum was detected by means of an AMPTECK XR-100T Cd-Te ϒ/X-ray detector with a diameter of 2 mm placed at a fixed angle with respect to the incident beam of 90° and phantom to detector distance of 50 mm. The phantom's face was placed at 45° with respect to the incident beam. The general setup is depicted in Fig. 2. The distance from the phantom's surface to the surface of the volume doped with Ag was varied from 1 mm to 15 mm emulating a tumorous volume at different depths in human tissue. In addition, the Ag concentration in the doped volume was varied from 0.005 to 0.05 M.

With a second setup, the feasibility of using Ag as a dopant agent for dose enhancement was studied with a similar configuration but removing both beam hardening filters. For that purpose, Fricke gel dosimeters containing silver NPs were placed at a depth of 1 mm and irradiated using an electrical current of 40 mA and voltage of 50 kVp obtaining a dose rate of 58.6 ± 0.3 cGy/min, which was measured with a Farmer type ionization chamber (PTW-Freiburg TN 30013) in water-equivalent phantoms. In order to evaluate if the dose enhancement caused mainly by the fluorescence of silver NPs could be determined by gel dosimetry. Cuvettes containing the same dosimetric material were irradiated using the same setup but with an incident beam with energies below the Ag K-edge using an incident spectrum with 25 kVp and an electrical current of 34.5 mA, resulting in a dose rate of 21.0 ± 0.1 cGy/min. For both cases the experimental conditions were designed for an absolute dose of 11.7 Gy in the Fricke gel dosimeter. This value was chosen as a suitable option to provide an optimal signal to background ratio in the spectra acquisition and at the same time in the sensitive dose region of the Fricke gel dosimetry (Valente et al., 2007; Vedelago et al., 2014).

The dose enhancement factor (DEF) was calculated as the ratio between the dosimeter readout of a sample doped with silver NPs irradiated at 50 kVp (I_{50kVp}) and at 25 kVp (I_{25kVp}).

$$DEF = \frac{I_{50kVp}}{I_{25kVp}} \quad (1)$$

Because contributions from L and M lines are negligible, the dose differences due to fluorescence are only present when the silver K-edge is excited with the 50 kVp beam.

2.3. Fricke gel dosimetry

The benzoic Fricke gel dosimeter (BFGD) sensitive material was manufactured based on the method described elsewhere (Vedelago et al., 2016). Briefly, benzoic acid (0.29% w/w) was dissolved at 60 °C distilled water with constant stirring, then gelatin 300 Bloom (2.90% w/w) was incorporated and stirred for 20 min at 50 °C. Then, sulfuric acid (1.39% w/w), xylenol orange (0.05% w/w), and ferrous sulfate (0.07% w/w) were added at 28 °C and stirred until a homogeneous solution was obtained. PMMA cuvettes of 10×10×20 mm^3 were filled with the dosimetric material and properly sealed to avoid the presence of oxygen during their storage, irradiation and post irradiation analyses. These materials were stored at 4 °C in a dark environment for at least 12 h before their irradiation. Ferrous sulfate and benzoic acid were provided by Research AG, (Buenos Aires, Argentina). The remaining reagents were purchased from Sigma Aldrich (Saint Louis, MO, USA) and used without further treatment.

To manufacture the BFGD dosimeters doped with silver NPs (Ag-BFGD), the reaction products were dialyzed using membranes with a molecular weight cutoff of 50 kD obtained from Spectrum Laboratories Inc. (Breda, The Netherlands). To that end, 5.0 mL of the reaction products samples were placed in a dialysis membrane and submerged into 500 mL of distilled water under mild stirring for 8 h, where solvent water exchange takes place. The dialysis solution was replaced with fresh distilled water every 22 h for a total exchange time of 96 h. The dialyzed product was then used to prepare BFGD dosimeters using the already described method but taking into account the gelatin contained in the silver NPs solution.

2.4. MC simulations

2.4.1. Simulation setup

The PENELOPE code system (version 2011) was used to perform the MC simulations (Baró et al., 1995) in this study. This code has been used and described extensively in numerous studies involving electron-photon transport and has been thoroughly validated against experimental data (Sempau et al., 2003). The simulated configuration was set to emulate the conditions used in the experimental section. Briefly, the configuration consisted on a point source emitting a conical beam placed at a source-to-surface distance (SSD) of 930 mm. A collimator of 30×30 mm^2 was placed 795 mm from the source forming an incident beam with a field size of 35.3×35.3 mm^2 on the phantom's surface. The incident spectrum used in the simulations was experimentally measured with the Amptek detector with a 50 μm diameter collimator on the Be window aligned with the incident beam and at the same SSD used in the simulations. It is worthwhile mentioning that with all these considerations, the distribution of emitted photons by the simulated source that reaches the phantom will have the same angular and energy distribution with the same field size used in the experiments. With the same idea, the geometry of the phantom was set according to the experimental setup. The composition of the simulated materials was built by means of the tools contained in the PENELOPE package. The default PENELOPE parameters for PET and PMMA were used; however, for the silver – water material different material properties were built for each Ag concentration.

The virtual detector used in the simulation was an impact detector

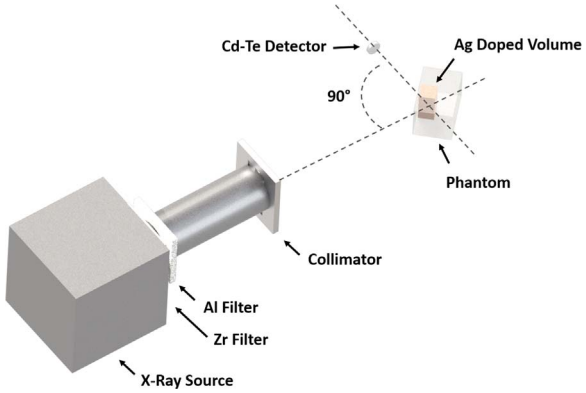

Fig. 2. Experimental irradiation setup.

with a 1 mm radius, which corresponds to the collimated area of the detector used in the experiments. It was placed at 50 mm and 45° with respect to the phantom's surface and it was set to quantify photons in energy bins of 1 eV.

All the simulations were carried out with 10^{10} primaries, in every case the statistical errors associated with the quantification of photons per bin were less than 10%. The remaining PENELOPE parameters were selected in order to reduce the calculation time without affecting significantly the obtained results. The parameters for the condensed simulation scheme are C1=C2=0.01, Wcc=1×10^4 eV y Wcr=1×10^3 eV. The cut-off energies used are Eabs=5×10^3 eV for e^- and e^+, Eabs=1×10^3 eV for photons. The simulations lasted approximately 15 days, running in a CPU with Intel® Core™ i7 950, 3.07 Ghz with 4 Gb RAM and Linux Kernel 2.6.32 64.

2.4.2. Virtual detector response

In order to compare experimental and simulated results, it becomes essential to determine the intensity of the fluorescence peaks relative to the intensity of the signal produced by dispersion photons like Compton and Rayleigh contributions. Since the energy distribution of the fluorescence peaks is practically monochromatic, the height or intensity of such peaks should be strongly dependent on the energy resolution of the detector (Leo, 1994). If a detector with a high energy resolution is used the fluorescence peaks would become more intense and would have a smaller full width at half maximum (FWHM). When performing MC simulations, the energy resolution of the detector can be varied and set to arbitrary values. However, in the experimental setup a fixed value is already established with the selected detector. Therefore, some strategy must be developed to convert the virtual detector resolution to the real one and then be able to compare the peaks intensity.

2.4.3. FWHM determination

The FWHM as a function of energy for the detectors like the one used in this study can be expressed as:

$$FWHM(E)=2.35\sqrt{Fw}\sqrt{E} \tag{2}$$

$$FWHM(E)=k\sqrt{E} \tag{3}$$

where w is the necessary average energy to produce an ionization, F is the Fano factor and k is a fitting constant.

In order to obtain a continuous function of FWHM with energy, the manufacturer reported FWHM values for the AMPTEK detector were fitted to the expression in Eq. (3), by means of the CurveFitting toolbox in Matlab® version 7.11.0.584 (R2010b) 64 bit (MathWorks Inc, Natick, MA, USA) obtaining a value of k=2.476 $eV^{0.5}$. Both manufacturer FWHM values and the fitted curve are presented in Fig. 3 as a function of the energy.

2.4.4. Virtual detector energy resolution

The quantification obtained with the virtual detector was adjusted to the real one by convoluting the virtual detector signal with a Gaussian filter as follows:

$$g(x)=\frac{1}{\sqrt{2\pi\sigma^2}}e^{\left(\frac{-x^2}{2\sigma^2}\right)} \tag{4}$$

And

$$\sigma(E)=\frac{FWHM(E)}{2.35}=\frac{k\sqrt{E}}{2.35} \tag{5}$$

Finally, for a given spectrum in the virtual detector f(E), the adjusted spectrum according to the experimental resolution is calculated by:

$$F_{real}(E)=\int f(x)g(x-E)dx=\frac{1}{\sqrt{2\pi\sigma^2}}\int f(x)e^{\left(\frac{-(x-E)^2}{2\sigma^2}\right)}dx \tag{6}$$

According to this fitting process, the energy dispersion is considered, but other effects like peak tailing, escape peaks, escape by Compton dispersion are not taken into account. However, these other effects are not really significant with the X-ray energies used in this study.

2.5. Comparison method

In order to compare simulations to experimental results, a background subtraction methodology was used, similar to the one used by other authors (Figueroa et al., 2015; Wu et al., 2013). Simulations and experiments without Ag were performed for every setup with the purpose of determining the scattering contribution to the spectrum. Then, this signal was subtracted from the spectra obtained with doped Ag samples, obtaining in that way the fluorescence contribution from each experiment and simulation. Kα peaks were used in this study mainly because the Compton signal overlaps with Kß peaks and also because Kß signals were much less intense than Kα ones.

Finally, curves with this information for different doped volume depths and different Ag concentrations were normalized and compared. The method used for the comparison of the measured (S_m) and simulated (S_s) emission spectra can be summarized as follows:

1. The Kα channels are identified, i.e. $E_{K\alpha}$.
2. A narrow interval around the Kα lines (δE), equivalent to the fluorescence peak, is considered as the interval of interest.

   $S_m(E_{K\alpha}-\delta E < E < E_{K\alpha}+\delta E)=\grave{S_m}$
3. The recorded signal in the channels already identified for the measured and simulated spectra obtained for a silver concentration of 0% is used as a background subtraction (mainly due to Compton scattering).

   $B_m^{0M}=S_m(0M)\ and\ B_s^{0M}=S_s(0M)$
4. The obtained signal, hereinafter referred to as relative intensity signal, is considered as the “net” or “pure” signal due to the presence of Ag.

   $\grave{S_m}-\grave{B_m^{0M}}$

   And

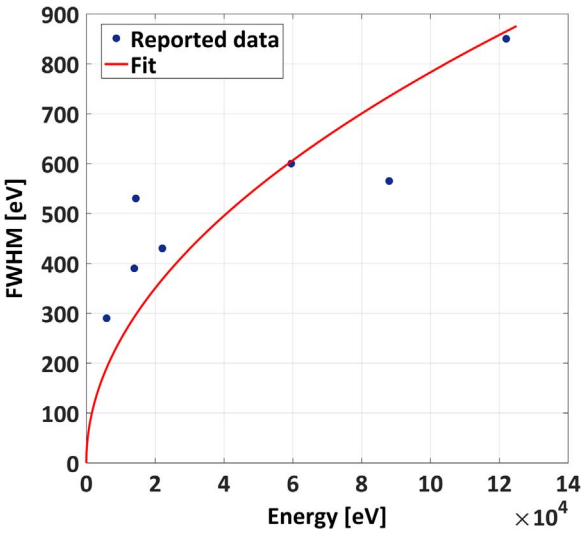

Fig. 3. FWHM vs Energy. Manufacturer reported data and fitted curve.

$\grave{S}_s - \grave{B}_s^{0M}$

5. The final step consists in normalizing the obtained results using one case as a reference for both simulated and experimental data, in order to use the same scale for comparison purposes.

$$\text{Normalized simualted relative intensity} = \frac{S_s^{\grave{x}M} - B_s^{\grave{0}M}}{(S_s^{\grave{x}M} - B_s^{\grave{0}M})_{REF}}$$

And

$$\text{Normalized measured relative intensity} = \frac{S_m^{\grave{x}M} - B_m^{\grave{0}M}}{(S_m^{\grave{x}M} - B_m^{\grave{0}M})_{REF}}$$

In this particular study, the reference case for either simulated or experimental data was set to the signal at 0.05 M of silver concentration. Uncertainties are assessed by conventional error propagation according to the scheme described above.

3. Results and discussion

3.1. Nanoparticle synthesis

The effect of variations of the $AgNO_3$ concentration on the NPs morphology and size distribution was studied by means of TEM. Fig. 4 shows TEM micrographs of the reaction products obtained with a 1% w/w gelatin concentration and two different initial $AgNO_3$ concentrations.

There is a clear difference in size and size distribution between both reaction products, where a higher Ag ion concentration leads to smaller particles and a narrower distribution, the analysis of a larger set of particles has been summarized in Fig. 5.

Larger concentrations of the Ag precursor lead to a much larger number of particles with a smaller mean particle size and narrower size distributions. Which in fact are desirable properties to obtain more stable suspensions in aqueous media and homogenous properties such as diffusion or effects related to the specific surface area of silver NPs.

From an experimental point of view, the homogeneity and stability obtained for solutions of silver salts is always better than the one that can be achieved with a suspension of silver NPs. Nevertheless, the fluorescence of these materials should not be different if the concentration of silver is the same. Furthermore, it is well known that the fluorescent emission is a specific quantum property of the irradiated material determined by the energy of the atomic levels involved in the transition. The effect is strongly dependent on the atomic number, whereas the influence of molecular binding and chemical environment only contribute to slight changes shifting the transition energies (Ceppi et al., 2013). In this context, the fluorescent emission due to the presence of silver atoms might be considered as being quite independent of the case in which silver is actually being part of NPs or part of $AgNO_3$ salt. Therefore, the fluorescent characteristic peaks in the recorded spectrum correspond to the total quantity of silver in the irradiation bulk. Nevertheless, NPs can be tuned and modified with polymers or organic compounds to have better biocompatibility (García-Ruiz et al., 2015; Neri et al., 2016) for radiotherapy applications while salts or metallic cations are not able to perform. In addition, in gel dosimetry the use of $AgNO_3$ is restricted for some materials such as Fricke gel since silver ions can oxidize Fe^{2+} ions and then modify the optical properties of the dosimeter together with the content of radiosensitive material. In Fig. 6, Fricke gel dosimeters prepared directly from the reaction mixture containing a mixture of silver NPs and silver ions are compared to dosimeters prepared with silver NPs dialyzed from those reaction products. Clearly, the use of silver salts has a severe effect on the Fricke gel material (Fig. 6E). On the other hand, the dosimeters prepared with the dialyzed NPs (Fig. 6C) have a slight darker color because of the optic nature of the nanoparticle suspension, but there is no evidence of a reaction in the mixture.

For the irradiation experiments, NPs obtained with a $AgNO_3$ initial concentration of 0.05 M was used. Thus, a silver nanoparticle suspension stabilized with gelatin with a mean area equivalent diameter of 6.33 nm and a standard deviation of 3.74 nm was used.

3.2. Silver fluorescence detection with X-rays

The intensity for the Kα lines at different depths and silver concentrations was determined experimentally with the setup described previously, where the detector was placed at a distance of 50 mm with respect to the phantom's surface and at an angle of 90° with respect to the incident beam. A clear distinction of the Kα lines was obtained with this configuration within the studied boundaries.

Scattering spectra in the region of interest near to the fluorescent Kα and Kß lines are presented in Fig. 7. The same methodology used with Kα signal could be applied to Kß; however, their low intensity together with a larger Compton signal in that energy range would lead to significant uncertainties. In this study, it was possible to identify silver concentrations in aqueous and tissue equivalent materials by using only the intensity of the Kα peaks. However, more reliability can be granted if multiple signals are used, e.g. Kα and Kß. In addition, for some particular cases like in complex situations with multiple fluorescent agents used for specific targeting or detection approaches, it may become one of the only alternatives.

With the information obtained from these spectra and by using the method described in section 2.6, two different effects were studied. First, changes in the intensity of Kα peaks against variations on the silver concentration of the samples and then the influence of the distance between the phantom's surface and the doped volume or

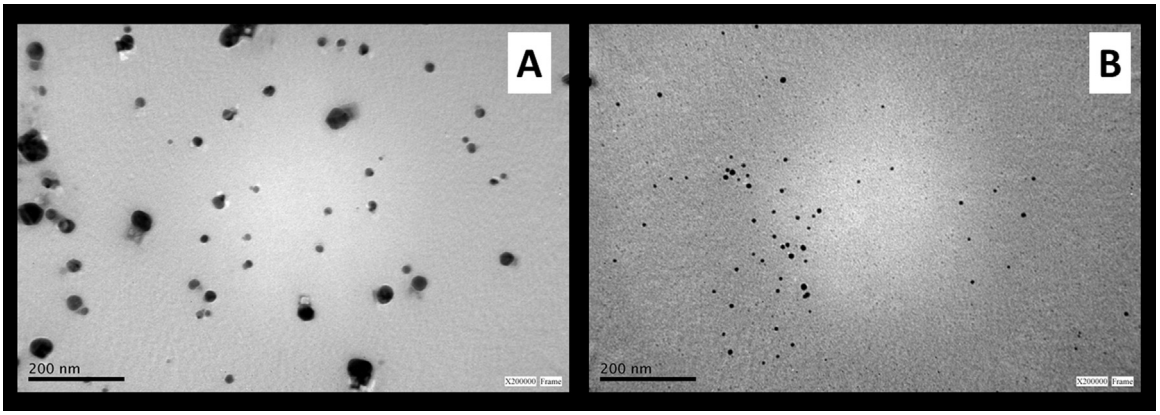

Fig. 4. TEM micrographs of the reaction products obtained with an initial $AgNO_3$ concentration of **A)** 0.025 M, **B)** 0.05 M.

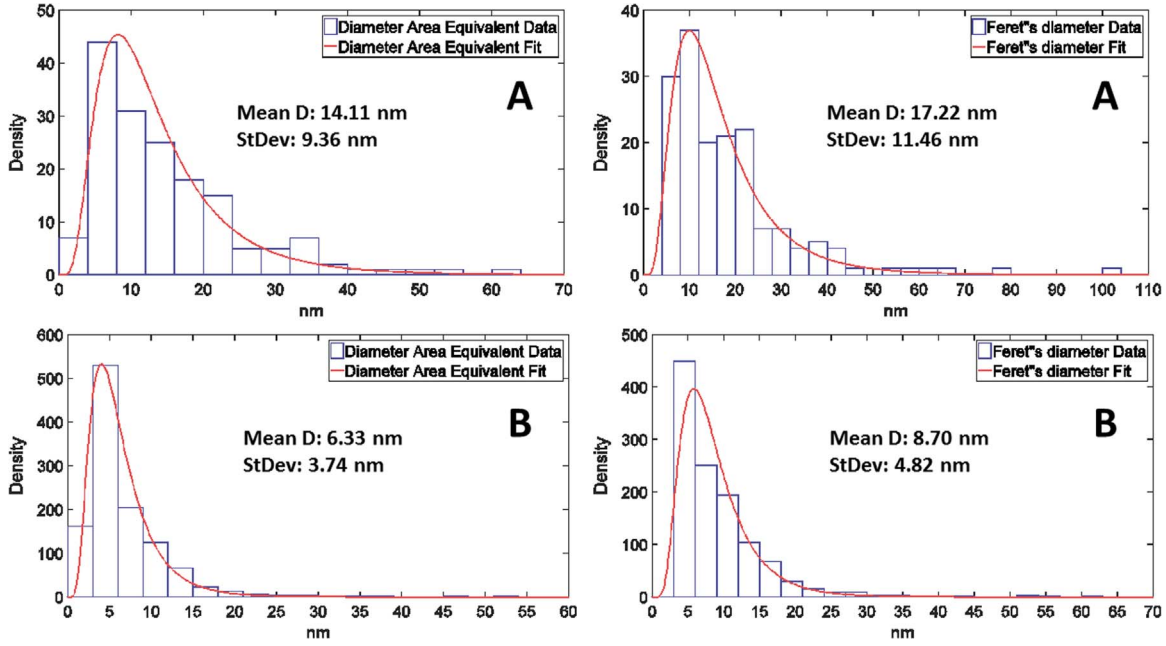

Fig. 5. Probability density functions (PDF) and fitted Lognormal distributions for the size descriptors of the reaction products obtained with an initial $AgNO_3$ concentration of **A)** 0.025 M, **B)** 0.05 M.

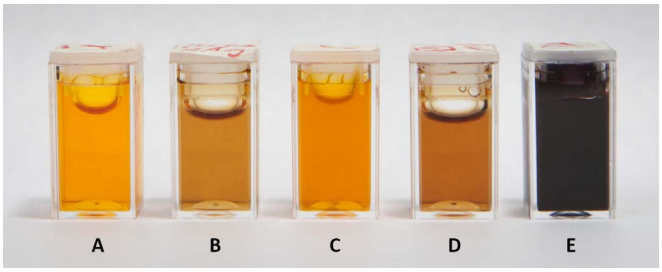

Fig. 6. A) BFGD dosimeter, **B)** dialyzed silver NPs, **C)** Ag-BFGD **D)** reaction product of $AgNO_3$ and gelatin, **E)** BFGD dosimeter doped with the reaction product of $AgNO_3$ and gelatin.

sample. The results of the former are presented in Fig. 8. The obtained subtracted spectra for different Ag concentrations at a depth from 1 mm to 15 mm presents a linear trend in the range of concentration used in this study, which is agreement with other authors (Alivov et al., 2014; Figueroa et al., 2015).

Nevertheless, if the concentration could be increased beyond the solubility limit of the salt solutions or the stability limit of the suspension of NPs, a saturation value would be reached for higher Ag concentrations, this statement is not easy to be measured experimentally but can be analyzed by means of MC simulations where materials with a silver concentration higher than the stability limit for the nanoparticle suspensions can be used as shown in Fig. 9, where the dashed line is a linear interpolation which has been added as a visual aid.

The effect of depth on the detectability of silver fluorescence in these materials is depicted in Fig. 10. The measured Kα intensity lines describe an exponential decrease with an increase in the depth of the doped volume within the phantom at the energies and irradiation conditions used in this study. The exponential fitting of every curve had a determination coefficient value (R^2) greater than 0.99. These results indicate that it is still possible to detect the presence of silver for concentrations as low as 0.005 M.

3.3. MC simulations

In order to proof if PENELOPE MC simulations could be used in X-ray irradiations with silver NPs the results obtained from the simulations and processed with the method proposed in section 2.6 were compared to the experimental results. For the simplest case, where the highest concentration of Ag was used both results are very approximate as depicted in Fig. 11. What is more, experimental results are contained within the error of the proposed simulation and calculation procedure. The error bars in the MC simulations could be narrowed if a larger number of primaries would have been used. However, it is worthwhile mentioning that the simulations of these results already

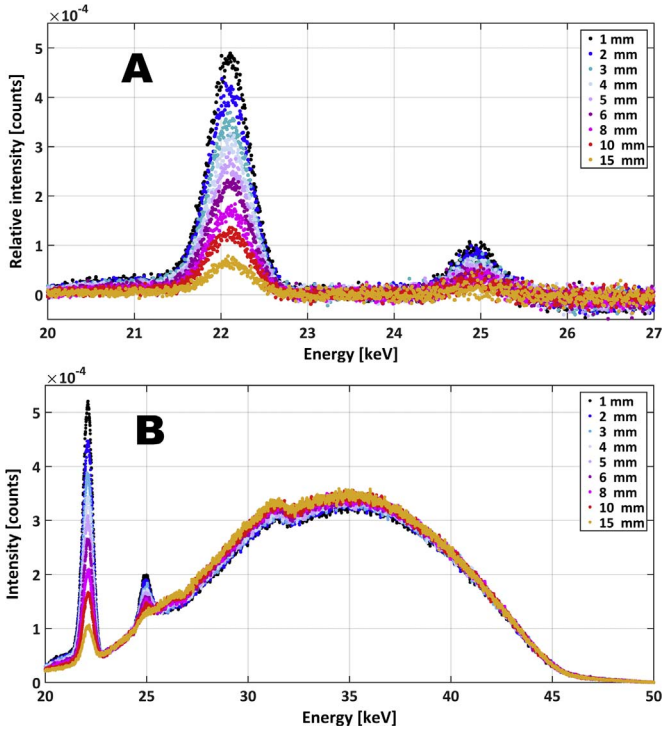

Fig. 7. A) Relative spectra in the fluorescence range of interest for a Ag concentration of 0.05 M at different depths. **B)** Compton contribution in the scattered spectra of samples with a Ag concentration of 0.05 M.

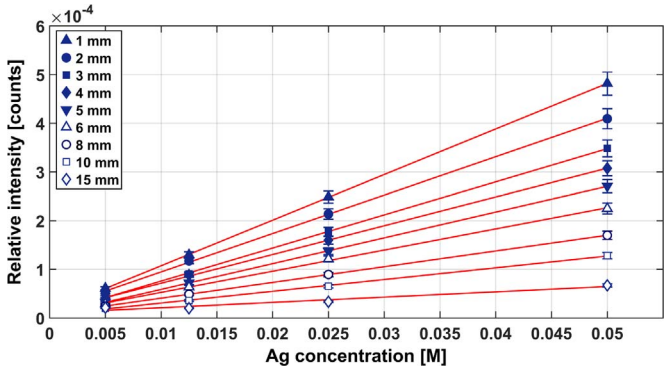

Fig. 8. Experimental relative Kα intensity lines vs Ag concentration for different Ag doped volume depths.

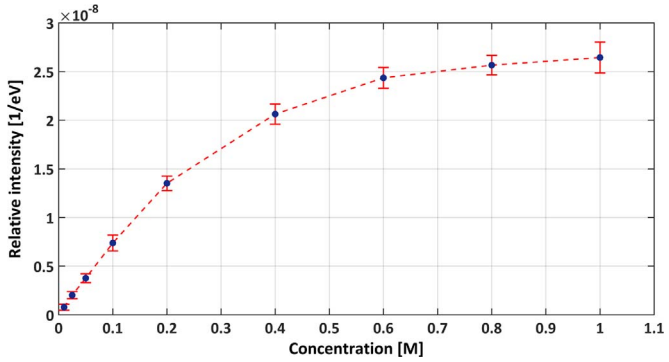

Fig. 9. MC simulation for high concentration of Ag at a doped volume depth of 1 mm.

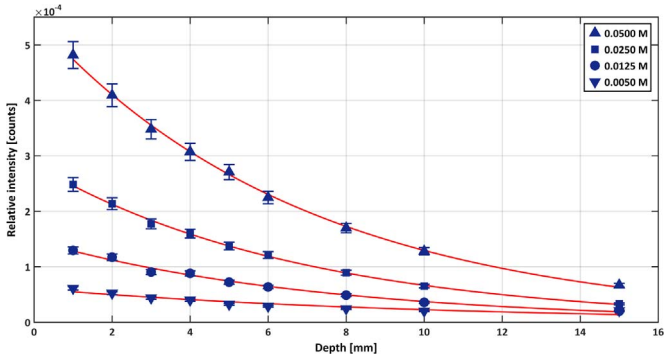

Fig. 10. Experimental relative Kα intensity lines vs Ag doped volume depth with different Ag concentrations.

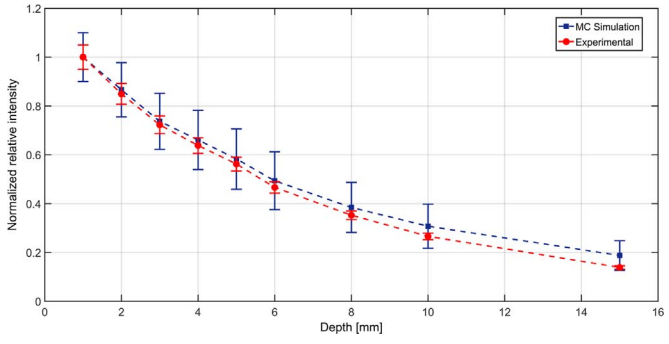

Fig. 11. Simulated and experimental normalized relative Kα intensity for a Ag concentration of 0.05 M at different depths.

require 15 days of computational work, and increasing the primaries in one order of magnitude from 10^{10} to 10^{11} would need approximately 150 days of calculation time.

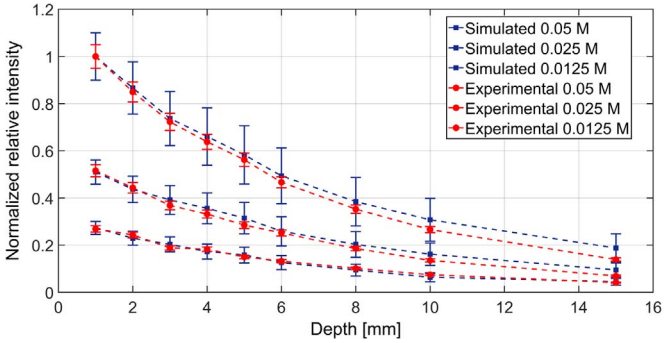

Fig. 12. Simulated and experimental normalized relative Kα intensity for Ag concentrations of 0.05 M, 0.025 M and 0.0125 M at different depths.

The effect of the two variables studied in the experiments with silver NPs, which are the metal concentration and the depth of the sample with NPs are accurately described by the MC simulations. In Fig. 12, three different Ag concentrations were simulated at different depths from 1 to 15 mm. These results are compared to the obtained in the experimental section. The errors of both experimental and simulated data correspond to one standard deviation.

Being able to simulate and predict the behavior of the fluorescence of silver NPs in a confined tissue equivalent volume present numerous advantages, such as studying complex setups with different concentrations, shapes and materials. Also, they provide the possibility to perform patient-specific simulations in like geometries inferred from CT images. From a research point of view, the use of simulations has the great advantage of discriminating physic contributions. For example, in an X-ray simulation, it is possible to study if the absorbed dose was deposited by photoelectrons, Auger electrons, Compton or secondary electrons. Lastly, in cases where the scattering radiation spectra are measured, it is possible to analyze the different contributions to the spectrum separately instead of doing a background subtraction method, e.g. discriminate Compton contribution from fluorescence.

3.4. Fricke gel dosimetry

Since the initial idea of using just silver ions to enhance the dosimetric sensitivity of a well-known and often used dosimetric system such as Fricke gel was not successful because of the oxidation of the ferrous ions against the silver salt. A feasibility test was carried out with silver NPs. A typical Fricke gel dosimeter was prepared with the obtained NPs in this study. No oxidation was observed before the irradiation of the materials and two different analyses were performed. First, the detectability of the silver NPs was measured by using the AMPTEK detector using the same setup already described for the rest of this study. The resulting relative intensity can be observed in Fig. 13.

Moreover, both materials were irradiated with different setups in order to have a total average dose of 11.7 Gy but with a different

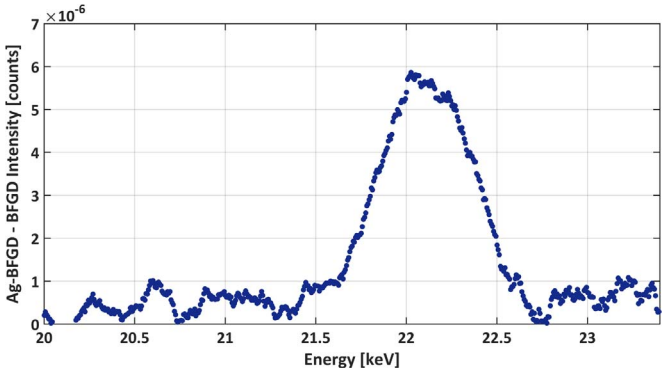

Fig. 13. Ag-BFGD scattered spectrum relative to BFGD.

incident beam energy of 25 kVp and 50 kVp. The dose enhancement as defined previously was 1.283, indicating an increase in the absorbed dose of 28.3% produced by the fluorescence of silver NPs. This result is only qualitative but is enough to prove the use of silver as a dosimetric enhancer and as a radiological sensitizer.

4. Conclusions

Silver nanoparticles with a mean characteristic size of 6.3 nm and a standard deviation of 3.4 nm were synthesized by a complexation – reduction method in a gelatin matrix, with the goal of obtaining a suitable and stable material for dosimetry in radiotherapy or radiodiagnostic applications. These materials were used to develop and validate a MC simulation tool which was able to reproduce the experimental relative intensity of the Kα peaks of samples with Ag concentrations from 0.005 to 0.05 M and at different depths from 1 to 15 mm. The detectability of silver in tissue equivalent materials was studied for low energy X-ray irradiations, obtaining an excellent agreement between both experimental and simulation methods. A comparison method has been proposed in order to normalize the relative intensities of every approach taken in this study. The normalization method includes the information of the spectra of the materials without the presence of inorganic substances, and a convolution method to correct the difference between the behavior of a real detector vs a virtual one. With this method, the relative intensity of the materials containing silver NPs resulting from the experiments and MC simulations were indistinguishable and lied within the uncertainties of the methods. Also, the effect of variations in the Ag concentration and in the depth of the doped volume was perfectly described by the simulations. Finally, a feasibility test of using these NPs as a dose enhancer in Fricke gel dosimetry was performed, proving that there is a signal increase of 28.3%.

Acknowledgements

This study was partially financed by CONICET by means of the Project ESPORA I - PIP 112-20130100658CO, PIP 112-0.20110101029, PIP 114-20090100398 and SeCyT-UNC by means of DOSCOM I project and INSPIRATE I program. This project was also partially supported by Universidad de La Frontera by DIUFRO DI 6008-16 project.

References

Alivov, Y., Baturin, P., Le, H.Q., Ducote, J., Molloi, S., 2014. Optimization of K-edge imaging for vulnerable plaques using gold nanoparticles and energy resolved photon counting detectors: a simulation study. Phys. Med. Biol. 59, 135–152. http://dx.doi.org/10.1088/0031-9155/59/1/135.

Baró, J., Sempau, J., Fernández-Varea, J.M., Salvat, F., 1995. PENELOPE: an algorithm for Monte Carlo simulation of the penetration and energy loss of electrons and positrons in matter. Nucl. Instrum. Methods Phys. Res. B 100, 31–46. http://dx.doi.org/10.1016/0168-583X(95)00349-5.

Barreto, J.A., O'Malley, W., Kubeil, M., Graham, B., Stephan, H., Spiccia, L., 2011. Nanomaterials: applications in cancer imaging and therapy. Adv. Mater. 23, H18–H40. http://dx.doi.org/10.1002/adma.201100140.

Botchway, S.W., Coulter, J.A., Currell, F.J., 2015. Imaging intracellular and systemic in vivo gold nanoparticles to enhance radiotherapy. Br. J. Radiol. 88, 1–13. http://dx.doi.org/10.1259/bjr.20150170.

Caschera, L., Lazzara, A., Piergallini, L., Ricci, D., Tuscano, B., Vanzulli, A., 2016. Contrast agents in diagnostic imaging: present and future. Pharmacol. Res. 110, 65–75. http://dx.doi.org/10.1016/j.phrs.2016.04.023.

Ceppi, S., Mesquita, A., Pomiro, F., Miner, E.V.P., Tirao, G., 2013. Study of Kβ X-ray emission spectroscopy applied to Mn (2 À x) V (1 þ x) O 4 (x¼ 0 and 1/3) oxyspinel and comparison with XANES. J. Phys. Chem. Solids 75, 366–373. http://dx.doi.org/10.1016/j.jpcs.2013.11.002.

Coppola, M., Vulpis, N., Bertoncello, G., 1984. Enhancement of chromosomal damage in human lymphocytes irradiated with X rays in the presence of iodine. Radiat. Prot. Dosim. 9, 99–104.

Figueroa, R.G., Santibañez, M., Malano, F., Valente, M., 2015. Optimal configuration for detection of gold nanoparticles in tumors using Kβ X-ray fluorescence line. Radiat. Phys. Chem. 117, 198–202. http://dx.doi.org/10.1016/j.radphyschem.2015.08.017.

García-Ruiz, A., Crespo, J., López-de-Luzuriaga, J.M., Olmos, M.E., Monge, M., Rodríguez-Álfaro, M.P., Martín-Álvarez, P.J., Bartolome, B., Moreno-Arribas, M.V., 2015. Novel biocompatible silver nanoparticles for controlling the growth of lactic acid bacteria and acetic acid bacteria in wines. Food Control 50, 613–619. http://dx.doi.org/10.1016/j.foodcont.2014.09.035.

Guidelli, E.J., Baffa, O., 2014. Influence of photon beam energy on the dose enhancement factor caused by gold and silver nanoparticles: an experimental approach. Med. Phys. 41, 032101. http://dx.doi.org/10.1118/1.4865809.

Hainfeld, J.F., Slatkin, D.N., Smilowitz, H.M., 2004. The use of gold nanoparticles to enhance radiotherapy in mice. Phys. Med. Biol. 49, 309–315. http://dx.doi.org/10.1088/0031-9155/49/18/N03.

Jones, B.L., Krishnan, S., Cho, S.H., 2010. Estimation of microscopic dose enhancement factor around gold nanoparticles by Monte Carlo calculations. Med. Phys. 37, 3809–3816. http://dx.doi.org/10.1118/1.3455703.

Kuang, Y., Pratx, G., Bazalova, M., Meng, B., Qian, J., Xing, L., 2013. First demonstration of multiplexed X-ray fluorescence computed tomography (XFCT) imaging. IEEE Trans. Med. Imaging 32, 262–267. http://dx.doi.org/10.1109/TMI.2012.2223709.

Lee, J., Yang, J., Kwon, S.G., Hyeon, T., 2016. Nonclassical nucleation and growth of inorganic nanoparticles. Nat. Rev. Mater. 1, 16034. http://dx.doi.org/10.1038/natrevmats.2016.34.

Leo, W.R., 1994. Techniques for Nuclear and Particle Physics Experiments: A How-to Approach. Springer-Verlag Berlin Heidelberg, Heidelberg, Germany.

Linic, S., Aslam, U., Boerigter, C., Morabito, M., 2015. Photochemical transformations on plasmonic metal nanoparticles. Nat. Mater. 14, 567–576. http://dx.doi.org/10.1038/nmat4281.

McMahon, S.J., Hyland, W.B., Muir, M.F., Coulter, J.A., Jain, S., Butterworth, K.T., Schettino, G., Dickson, G.R., Hounsell, A.R., O'Sullivan, J.M., Prise, K.M., Hirst, D.G., Currell, F.J., 2011. Biological consequences of nanoscale energy deposition near irradiated heavy atom nanoparticles. Sci. Rep. 1, 1–18. http://dx.doi.org/10.1038/srep00018.

Mohanraj, V., Chen, Y., Chen, M., 2006. Nanoparticles – a review. Trop. J. Pharm. Res Trop. J. Pharm. Res 5, (561–561).

Nath, R., Bongiorni, P., Rockwell, S., 1990. Iododeoxyuridine radiosensitization by low- and high-energy photons for brachytherapy dose rates Iododeoxyuridine radiosensitization by low-and high-energy photons for brachytherapy dose rates'. Radiat. Res. 124, 249–258.

Neri, F., Scala, A., Grimato, S., Santoro, M., Spadaro, S., Barreca, F., Cimino, F., Speciale, A., Saija, A., Grassi, G., Fazio, E., 2016. Biocompatible silver nanoparticles embedded in a PEG–PLA polymeric matrix for stimulated laser light drug release. J. Nanopart. Res 18 (153), 1–14. http://dx.doi.org/10.1007/s11051-016-3467-1.

Nie, Z., Petukhova, A., Kumacheva, E., 2010. Properties and emerging applications of self-assembled structures made from inorganic nanoparticles. Nat. Nanotechnol. 5, 15–25. http://dx.doi.org/10.1038/nnano.2009.453.

Pan, K., Zhong, Q., 2016. Organic nanoparticles in foods: fabrication, characterization, and utilization. Annu. Rev. Food Sci. Technol. 7, 245–266. http://dx.doi.org/10.1146/annurev-food-041715-033215.

Petros, R.A., DeSimone, J.M., 2010. Strategies in the design of nanoparticles for therapeutic applications. Nat. Rev. Drug Discov. 9, 615–627. http://dx.doi.org/10.1038/Nrd2591.

Puntes, V., 2016. Design and pharmacokinetical aspects for the use of inorganic nanoparticles in radiomedicine. Br. J. Radiol. 89, 20150210. http://dx.doi.org/10.1259/bjr.20150210.

Rancoule, C., Magné, N., Vallard, A., Guy, J.-B., Rodriguez-Lafrasse, C., Deutsch, E., Chargari, C., 2016. Nanoparticles in radiation oncology: from bench-side to bedside. Cancer Lett. 375, 256–262. http://dx.doi.org/10.1016/j.canlet.2016.03.011.

Regulla, D.F., Hieber, L.B., Seidenbusch, M., 1998. Physical and biological interface dose effects in tissue due to X-ray-induced release of secondary radiation from metallic gold surfaces. Radiat. Res. 150, 92–100. http://dx.doi.org/10.2307/3579649.

Rice, S.B., Chan, C., Brown, S.C., Eschbach, P., Han, L., Ensor, D.S., Stefaniak, A.B., Bonevich, J., Vladár, A.E., Hight Walker, A.R., Zheng, J., Starnes, C., Stromberg, A., Ye, J., Grulke, E.A., 2013. Particle size distributions by transmission electron microscopy: an interlaboratory comparison case study. Metrologia 50, 663–678. http://dx.doi.org/10.1088/0026-1394/50/6/663.

Sancey, L., Lux, F., Kotb, S., Roux, S., Dufort, S., Bianchi, A., Crémillieux, Y., Fries, P., Coll, J.-L., Rodriguez-Lafrasse, C., Janier, M., Dutreix, M., Barberi-Heyob, M., Boschetti, F., Denat, F., Louis, C., Porcel, E., Lacombe, S., Le Duc, G., Deutsch, E., Perfettini, J.-L., Detappe, A., Verry, C., Berbeco, R., Butterworth, K.T., McMahon, S.J., Prise, K.M., Perriat, P., Tillement, O., 2014. The use of theranostic gadolinium-based nanoprobes to improve radiotherapy efficacy. Br. J. Radiol. 87, 20140134. http://dx.doi.org/10.1259/bjr.20140134.

Sau, T.K., Rogach, A.L., 2010. Nonspherical noble metal nanoparticles: colloid-chemical synthesis and morphology control. Adv. Mater. 22, 1781–1804. http://dx.doi.org/10.1002/adma.200901271.

Sau, T.K., Rogach, A.L., Jäckel, F., Klar, T.A., Feldmann, J., 2010. Properties and applications of colloidal nonspherical noble metal nanoparticles. Adv. Mater. 22, 1805–1825. http://dx.doi.org/10.1002/adma.200902557.

Schreiner, L.J., 2004. Review of Fricke gel dosimeters. J. Phys. Conf. Ser. 3, 9–21. http://dx.doi.org/10.1088/1742-6596/3/1/003.

Schütz, C.A., Juillerat-Jeanneret, L., Mueller, H., Lynch, I., Riediker, M., 2013. Therapeutic nanoparticles in clinics and under clinical evaluation. Nanomedicine 8, 449–467. http://dx.doi.org/10.2217/nnm.13.8.

Sempau, J., Fernández-Varea, J.M., Acosta, E., Salvat, F., 2003. Experimental benchmarks of the Monte Carlo code PENELOPE. Nucl. Instrum. Methods Phys. Res. B 207, 107–123. http://dx.doi.org/10.1016/S0168-583X(03)00453-1.

Smith, L., Kuncic, Z., Ostrikov, K., (Ken), Kumar, S., 2012. Nanoparticles in cancer imaging and therapy. J. Nanomater. 2012, 1–7. http://dx.doi.org/10.1155/2012/891318.

Taupin, F., Flaender, M., Delorme, R., Brochard, T., Mayol, J.-F., Arnaud, J., Perriat, P., Sancey, L., Lux, F., Barth, R.F., Carrière, M., Ravanat, J.-L., Elleaume, H., 2015. Gadolinium nanoparticles and contrast agent as radiation sensitizers. Phys. Med. Biol. 60, 4449–4464. http://dx.doi.org/10.1088/0031-9155/60/11/4449.

Thakor, A.S., Jokerst, J., Zavaleta, C., Massoud, T.F., Gambhir, S.S., 2011. Gold nanoparticles: a revival in precious metal administration to patients. Nano Lett. 11, 4029–4036. http://dx.doi.org/10.1021/nl202559p.

Titus, D., Samuel, E.J.J., Mohana Roopan, S., 2016. Current scenario of biomedical aspect of metal-based nanoparticles on gel dosimetry. Appl. Microbiol. Biotechnol. 100, 4803–4816. http://dx.doi.org/10.1007/s00253-016-7489-5.

Valente, M., Aon, E., Brunetto, M., Castellano, G., Gallivanone, F., Gambarini, G., 2007. Gel dosimetry measurements and Monte Carlo modeling for external radiotherapy photon beams: comparison with a treatment planning system dose distribution. Nucl. Instrum. Methods Phys. Res. Sect. A Accel. Spectrom. Detect. Assoc. Equip. 580, 497–501. http://dx.doi.org/10.1016/j.nima.2007.05.243.

Vedelago, J., Obando, D.C., Malano, F., Conejeros, R., Figueroa, R., Garcia, D., González, G., Romero, M., Santibañez, M., Strumia, M.C., Velásquez, J., Mattea, F., Valente, M., 2016. Fricke and polymer gel 2D dosimetry validation using Monte Carlo simulation. Radiat. Meas. 91, 54–64. http://dx.doi.org/10.1016/j.radmeas.2016.05.003.

Vedelago, J., Quiroga, A., Valente, M., 2014. Characterization of ferric ions diffusion in Fricke gel dosimeters by using inverse problem techniques. Radiat. Eff. Defects Solids 169, 845–854. http://dx.doi.org/10.1080/10420150.2014.958749.

Weissleder, R., Nahrendorf, M., Pittet, M.J., 2014. Imaging macrophages with nanoparticles. Nat. Mater. 13, 125–138. http://dx.doi.org/10.1038/nmat3780.

Wildgoose, G.G., Banks, C.E., Compton, R.G., Compton, R.G., 2006. Metal nanoparticles and related materials supported on carbon nanotubes: methods and applications. Small 2, 182–193. http://dx.doi.org/10.1002/smll.200500324.

Wu, D., Li, Y., Wong, M.D., Liu, H., 2013. A method of measuring gold nanoparticle concentrations by X-ray fluorescence for biomedical applications. Med. Phys. 40 (051901), 10. http://dx.doi.org/10.1118/1.4798966.

Yamada, M., Foote, M., Prow, T.W., 2015. Therapeutic gold, silver, and platinum nanoparticles. Wiley Interdiscip. Rev. Nanomed. Nanobiotechnol. 7, 428–445. http://dx.doi.org/10.1002/wnan.1322.